JOURNAL OF PROPULSION AND POWER
Vol. 23, No. 5, September–October 2007

Internal Flowfield Investigation of a Hypersonic Inlet at Mach 6 with Bleed

J. Häberle* and A. Gülhan†
DLR, German Aerospace Center, Linder Höhe, 51147 Cologne, Germany

DOI: 10.2514/1.29669

To study the influence of viscous effects on the performance and, especially the internal flowfield, of scramjet engines, an experimental study has been carried out on a fixed geometry scramjet inlet operating at Mach 6. The tests have been performed using a hypersonic blowdown wind-tunnel facility. To reduce the risk of inlet unstart, a passive boundary-layer bleed has been integrated at the throat and successfully tested. The passive bleed reduces the lip shock-induced separation bubble on the ramp significantly. The obtained experimental results are discussed and compared with computational fluid dynamics calculations. To investigate the compression behavior, different backpressures have been applied and the effects on the internal flow structure are analyzed by means of schlieren pictures and pitot-pressure profiles at the exit of the isolator. The increased backpressure leads to a nonuniform change in pitot pressure and calculated Mach number profile based on the geometrical shape of the internal flowpath. The heat transfer coefficient to the inner sidewall of the isolator is calculated using the time-dependent surface temperature, measured with an infrared system. The variation of the Stanton number based on different flow phenomena could be resolved successfully.

Nomenclature

A	=	area, m^2
Bi	=	Biot number, $Bi = \alpha L_0 \cdot \lambda^{-1}$
C_P	=	specific heat capacity at constant pressure, $Jkg^{-1}K^{-1}$
C_V	=	specific heat capacity at constant volume, $Jkg^{-1}K^{-1}$
c_p	=	pressure coefficient $c_P = (p - p_\infty) \cdot q_\infty^{-1}$
dt	=	time step, s
I	=	internal compression, $I = 1 - (A_{\text{th}} \cdot A_{\text{lip}}^{-1})$
L_0	=	characteristic length, m
M	=	Mach number
m_{CR}	=	inlet mass capture ratio
p	=	pressure, Nm^{-2}
q	=	dynamic pressure, Nm^{-2}
$\dot{q}$	=	heat flux rate, Wm^{-2}
R	=	specific gas constant for air, $R = 287.15,\ Jkg^{-1}K^{-1}$
St	=	Stanton number, $St = \dot{q}_{\text{conv}}/\rho_\infty v_\infty c_{P,\text{air}}(T_{\text{rec}} - T_w)$
T	=	temperature, K
α	=	heat transfer coefficient, $Wm^{-2}K^{-1}$, calibration value
Δ	=	throttle degree, $\Delta = [1 - (A_{\text{mfm,th}}/A_0)] \cdot 100$
λ	=	heat conductivity, $Wm^{-1}K^{-1}$
ρ	=	density, kgm^{-3}

Subscripts and Superscripts

conv	=	convective
mfm	=	mass flow meter
rec	=	recovery
th	=	throat
$t0$	=	wind-tunnel total conditions
w	=	wall
∞	=	wind-tunnel freestream conditions

I. Introduction

THE propulsion unit is one of the critical subsystems for future hypersonic single-stage-to-orbit (SSTO) and two-stage-to-orbit (TSTO) space vehicles enabling access to space or hypersonic transportation [1]. The scientific goal is to investigate the components, i.e., inlet, isolator, combustion chamber, and nozzle of a complete scramjet engine numerically and experimentally and look at the implications of these specific results for an overall system design. Some of the activities performed in 2006 at German universities are summarized by Weigand et al. [2]. The overall design philosophy is divided into two main trends and is mainly driven by the purpose of the system; an excellent overview of RAM/scramjet systems is given by Fry [3]. For SSTO and TSTO systems, more or less two-dimensional propulsion systems are required. In contrast, for missile applications, axisymmetric shapes are a valid option. The design methodology of streamline tracing is presented by Billig and Kothari [4] for developing planar and axisymmetric inlets. The present paper focuses on the internal compression part of a two-dimensional scramjet system.

The internal flowpath of the compression system features some very complex flow phenomena like shock–shock interaction, shock–boundary-layer interaction, separation, and so on. Furthermore, the isolator connects the inlet with the combustion chamber and adapts the flow in terms of static pressure delivered by the inlet to the static pressure in the combustion chamber. This is accomplished by a so-called shock train, a system of oblique or normal shocks. An engineering relationship between the shock-train pressure rise as a function of the correlation parameter (including isolator length, Reynolds number, etc.) has been developed by Billig [5] and is also reported in Heiser and Pratt [6]. The effects of different inlet-isolator configurations, i.e., moveable cowl, different cowl geometry, and variable isolator length, is discussed in great detail by Emami et al. [7] including unstart/start phenomena by means of static pressure

Presented as Paper 8139 at the 14th AIAA/AHI International Space Planes and Hypersonic Systems and Technologies Conference, Canberra, Australia, 6–9 November 2006; received 9 January 2007; accepted for publication 2 April 2007.

*Ph.D. Student, Wind Tunnel Department of the Institute of Aerodynamic and Flow Technology. Student AIAA Member.

†Head of Department, Wind Tunnel Department of the Institute of Aerodynamic and Flow Technology. AIAA Member.

distribution. The operational characteristics in terms of pressure rise for a mixed compression inlet are explored in this technical paper. Among others, the results indicate that inlet unstart is more affected by shock–boundary-layer interaction than contraction ratio and captured mass flow.

The visualization of the complex internal flowfield for different backpressures at relatively low Mach numbers and total flow conditions has been discussed and compared with numerical computations previously by Hermann and Koschel [8] and Reinartz and Hermann [9]. The results show that the ramp separation bubble forms to a completely separated flow shortly before the inlet blocks. The increase of the isolator length leads to a higher obtainable throttle degree, up to a maximum value. After this maximum length is reached, a further increase does not affect the maximum throttle degree. The question of how different Mach numbers affect the shock-train structure and the wall pressure fluctuations in a rectangular duct have been discussed by Sugiyama and Minato [10]. For $M = 2$ flow conditions, a λ-type shock structure with symmetric geometry occurs. In contrast, for the $M = 4$ condition, asymmetric X-type shock structures are present. This shows altogether that the internal flowfield of hypersonic compression systems contains a great deal of physical flow phenomena which still have to be investigated in more detail.

This paper presents the results of the research subproject, which deals with the experimental investigation of hypersonic mixed-compression-type inlets, mainly by means of pressure measurement, schlieren, and, especially, infrared optical measurement techniques. The current work focuses on the internal part of a hypersonic mixed compression inlet, i.e., the isolator and the throat area.

The inlet consists of a two-dimensional double wedge ramp configuration with a horizontal lip. Thus the flow is turned outward from the centerline by two oblique shocks based on the geometry and is turned back into the freestream direction by a single lip shock. This configuration results in a strong lip shock impinging on the ramp boundary layer. Because the pressure gradient in the x direction is too large, the boundary layer separates and a large separation bubble emerges in the throat of the inlet. This separation bubble causes pressure losses and, more important, the risk of blocking the inlet during flight conditions. This can occur at different angles of attack, real flight total temperature, and total pressure conditions as well as for different ratios of wall to freestream temperature, changing the boundary-layer development [11]. Therefore, measures have to be taken to reduce this separation bubble. In addition, a parametric study is important, because the temperature ratio, for example, could be different in ground testing or a possible propulsion flight experiment, compared with the aimed acceleration space launcher stage. For all cases, the separation bubble must not lead to inlet unstart. In the present configuration, a passive boundary-layer bleed is integrated into the throat area as one option to control the viscous flow effects. Bleeding can control the boundary-layer growth and shock-induced boundary-layer separation as shown in several papers [12–16] for lower Mach numbers. The efficiency of bleed in the Mach 6 inlet model will be discussed in the present paper.

The flow structure in the isolator varies depending on the combustion chamber static pressure. These different structures are investigated and discussed in this paper by means of pitot pressure measurements, static pressure measurements, and schlieren technique. In addition, the first results of the calculated heat transfer coefficient on the isolator side walls by means of infrared thermography are presented. For discrete points, the temperature history is matched with analytical solutions of the unsteady Fourier equation for the flat plate to check the feasibility of the measured results. Tests on a complete two-dimensional propulsion system were performed by Kanda et al. [17] at Mach 6, including pressure profile and heat flux profile calculated from thermocouple measurements along the x axis.

Finally, the measured static pressures are compared with the results of two-dimensional computational fluid dynamics (CFD) computations. These computations have been performed with the commercial CFD code FLUENT and the implemented two-equation k–ω–shear stress transport (SST) turbulence model. More detailed three-dimensional calculations have been performed by Krause et al. [18] in the numerical subproject within the graduate college, including different wall temperatures.

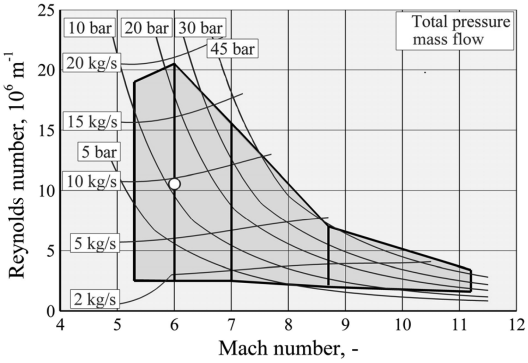

Fig. 1 Hypersonic wind-tunnel H2K performance map, including present trajectory point.

II. Experimental Tools

A. Wind-Tunnel and Test Conditions

All of the experiments discussed in this paper have been performed in the Hypersonic Wind Tunnel (H2K) at the German Aerospace Center in Cologne, Germany. The facility is a blowdown wind tunnel with test durations, depending on the flow conditions, of up to 30 s. The facility is equipped with five contoured nozzles with an exit diameter of 600 mm, i.e., $M = 5.3$, 6, 7, 8.7, 11.2. For the experiments of this study, the Mach 6 nozzle was used. To avoid condensation and to operate the wind tunnel at different stagnation temperatures, the air is heated by electrical heaters with a heating capacity of up to 5 MW. During the heating process, the air is blown out into the atmosphere until the desired stationary stagnation temperature is reached; subsequently, a 3/2 valve is activated to let the air flow through the nozzle into the vacuum dump tank. The range of achievable Mach numbers and Reynolds numbers, as well as a picture of the test section, can be seen in Fig. 1. Reynolds numbers between $2.5 \cdot 10^6$ m^{-1} to $20 \cdot 10^6$ m^{-1} can be set by varying the stagnation pressure and stagnation temperatures.

Assuming a flight Mach number of $M = 7$ for a possible hypersonic acceleration vehicle and a forebody ramp angle of 5.5 deg, the inlet faces Mach 6 flow conditions. Therefore, tests have been carried out at $M = 6$. The wind-tunnel flow conditions are summarized in Table 1.

B. Inlet Model

Throughout the presented campaign, an existing model called SCR-02 was used. The inlet configuration was designed as a self-starting inlet with a reduced internal compression of $I = 16\%$. This is well below the Kantrowitz and Donaldson [19] limit, which is $I = 32\%$ for the corresponding lip Mach number. To achieve this reduced internal compression and maintain the horizontal lip, the throat height is increased, resulting in a reduced second ramp as seen in Fig. 2. The second ramp and the horizontal throat are connected through an arc.

The SCR-02 configuration leads to a separation bubble in the throat region of the inlet resulting from the strong lip shock

Table 1 Wind-tunnel flow conditions

Wind-tunnel parameter	Value
Total temperature T_{t0}, K	481
Total pressure p_{t0}, Pa	$11.7942 \cdot 10^5$
Freestream Mach number M_∞	6
Freestream pressure p_∞, Pa	747
Freestream temperature T_∞, K	58.6
Freestream density ρ_∞, kgm^{-3}	0.0444
Unit Reynolds number Re_m, m^{-1}	$10.55 \cdot 10^6$

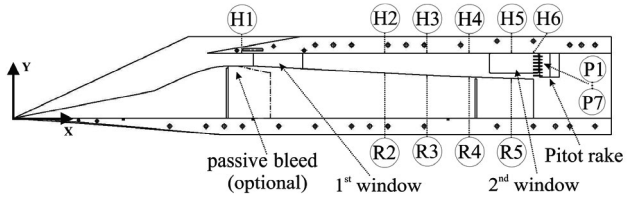

Fig. 2 Side view of inlet model with integrated passive bleed gap at the throat.

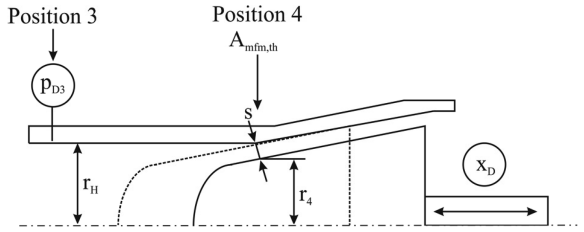

Fig. 3 Schematic view of conical mass flow meter.

impinging on the ramp boundary layer. This separation bubble may lead to inlet unstart. Therefore, the model was modified and a passive boundary-layer bleed was integrated (see the dash–dot line in Fig. 2). The bleed slot width and length in flow direction are 90×15 mm, respectively.

The capture cross section area A_0 of the model is 100×100 mm and the overall length is $L = 700$ mm. It is equipped with a pitot rake consisting of seven pitot tubes (P1–P7), ten static pressure ports in the isolator (H1–H6 and R2–R5), and, in total, four optical windows, which are integrated right after the throat area (first window) and at the end of the isolator (second window) for optical access (see Fig. 2). The inlet model is attached to the settling chamber of the flow meter. Depending on the optical measurement used, the inlet is either aligned in a way that the quartz windows are visible to the schlieren visualization setup or rotated around the x axis by 90 deg to allow optical access for the infrared system.

The internal part of the inlet from the throat to the end of the model is called the isolator, although the divergence of its geometry with an opening angle of −3 deg is too large. This shape is based on previous experimental requirements and could not be changed.

III. Measurement Techniques and Data Reduction

The hypersonic wind-tunnel facility is equipped with a coincident schlieren optic setup to visualize the flow around and in the inlet model. The use of a very light-sensitive charge-coupled device (CCD) camera allowed the modification of the optical path from a prism to a beam-splitter schlieren setup [20].

The static pressures, as well as the pitot pressure measurements, are made with the commercial Pressure Systems, Inc., 8400 system using a 32 psi module in the present investigation.

A. Flow Meter and Backpressure

To simulate the pressure induced by the combustion chamber and to measure the captured flow rate, a rotational symmetric flow meter with a conical plug was used [21]. The theory, which is used to evaluate the mass flow rate, assumes a one-dimensional flow without heat addition and sonic condition at the throat.

The whole device has been calibrated in advance according to the German Industrial Standard DIN-1952. Throughout the region of interest, the values of the calibration factor α vary between $0.99 < \alpha < 1.02$.

The mass capture ratio of the inlet is defined as

$$m_{\mathrm{CR}} = \alpha \frac{\dot{m}_{\mathrm{inlet,exit}}}{\dot{m}_0} \tag{1}$$

The calculation of the captured mass flow can be divided into three steps.

First, the throat area (position 4) of the flow meter is calculated based on the measured lateral position of the conical plug and the known geometrical dimensions of the mass flow meter (Fig. 3) according to

$$A_{\mathrm{mfm,th}} = \pi \cdot s \cdot (r_H + r_4) \tag{2}$$

Second, the Mach number ahead of the conical plug (position 3) is iteratively calculated by solving the following equation:

$$\frac{A_{\mathrm{mfm3}}}{A_{\mathrm{mfm,th}}} = \frac{1}{M_{\mathrm{mfm3}}} \left(\frac{1 + [(\kappa - 1)/2] M^2_{\mathrm{mfm3}}}{(\kappa + 1)/2} \right)^{(\kappa+1)/2(\kappa-1)} \tag{3}$$

Finally, the captured mass flow is calculated using the measured static pressure in front of the conical plug, the calculated Mach number, and the known total temperature, according to Eq. (4). The static pressure is measured at four locations on the circumference of the settling chamber (position 3) and averaged.

$$\dot{m}_{\mathrm{mfm}} = \frac{p_{\mathrm{mfm3}}}{\sqrt{R T_{t0}}} A_{\mathrm{mfm3}} \sqrt{\kappa} M_{\mathrm{mfm3}} \sqrt{\left(1 + \frac{\kappa - 1}{2} M^2_{\mathrm{mfm3}}\right)} \tag{4}$$

The theoretically captured mass flow can be calculated by the well-known total conditions in the freestream and the capture area of the inlet. Finally, the mass capture ratio is corrected by means of the calibration function to determine the correct captured mass flow, Eq. (1).

In addition to evaluating the captured mass flow of the inlet, the mass flow meter is also used to apply different backpressures to the inlet flow. This is achieved by reducing the throat area of the flow meter. The relation between the throttle degree Δ defined as

$$\Delta = \left(1 - \frac{A_{\mathrm{mfm,th}}}{A_0}\right) \cdot 100 \tag{5}$$

and the backpressure ratio can be seen in Fig. 4. The backpressure is measured at the pitot rake position, because this is defined to be the location of the interface between the "isolator" and the "combustion chamber." Without any backpressure imposed by the mass flow meter $\Delta < 40\%$, the static pressure ratio at the position of the pitot rake is $p/p_\infty = 10$. This very low value is based on the geometric shape of the isolator as described earlier. At $\Delta \approx 75\%$, which corresponds to a $p/p_\infty = 10$, there is still supersonic flow in the inlet throat and the inlet is started, but all of the isolator is subsonic. The pressure ratio in general increases with increasing throttling degree. However, there is a plateau in the range of $53 < \Delta < 62\%$, which must be due to the different shock structures in the settling chamber and the associated occurring of different pressure losses. For $\Delta > 67\%$, the flow at the exit of the isolator entering the settling chamber is completely subsonic. Thus there are no shocks present anymore and a further increase in throttling degree results in an almost linear increase of the backpressure ratio.

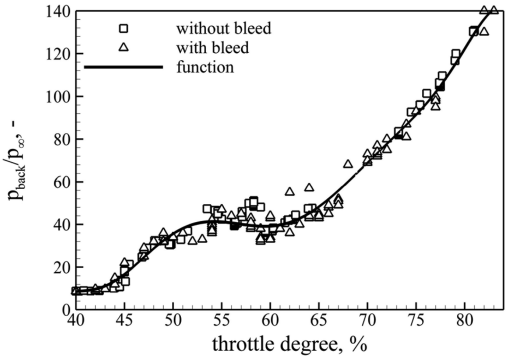

Fig. 4 Backpressure ratio as a function of throttling degree.

B. Side Wall Heat Flux Calculation

The estimation of the heat loads acting on a hypersonic inlet is of great importance to the overall system design, particularly for the choice of the material and the cooling concept. This especially plays a role for the internal areas of the propulsion system, because radiation cooling is not possible. One way to determine the heat flux to the wall is to measure the surface temperature history and use these data as boundary conditions for the numerical integration of the one-dimensional unsteady heat equation, Eqs. (6) and (7), in the direction normal to the surface [22]. Because thermocouples only measure at discrete points and the integration into the model surface might cause problems in terms of thermal insulation, as well as the heat conductivity/capacity of the thermocouple itself, the surface temperature distribution over time is measured with an infrared system [23], processed and stored in a three-dimensional array DATA$[x, y, t]$.

$$\rho(T)c_V(T)\frac{\partial T}{\partial t} = \frac{\partial}{\partial n}\left(\lambda(T)\frac{\partial T}{\partial n}\right) \tag{6}$$

$$\rho(T)c_V(T)\frac{\partial T}{\partial t} = \frac{\partial \lambda(T)}{\partial n}\frac{\partial T}{\partial n} + \lambda(T)\frac{\partial^2 T}{\partial n^2}$$

$$\Rightarrow \rho(T)c_V(T)\frac{\partial T}{\partial t} = \frac{\partial \lambda(T)}{\partial T}\left(\frac{\partial T}{\partial n}\right)^2 + \lambda(T)\frac{\partial^2 T}{\partial n^2} \tag{7}$$

Knowing the temperature distribution perpendicular to the wall, the temperature gradient can be evaluated and thus, the heat flux into the wall can be calculated. For external surfaces, the heat radiated from the surface has to be taken into account because the convective heat from the gas to the surface is the sum of radiated and conducted heat. For internal surfaces, like in the present case, the radiation is neglected based on the small differences in surface temperatures of the surrounding surfaces and the small viewing factor.

Because a one-dimensional approach is used, any heat fluxes in the plane of the investigated surface have to be minimized. This is accomplished by the use of a weak heat conducting material, i.e., PEEK. The use of this material insures that the thermal gradient normal to the surface is dominant and that the smearing of the temperature distribution can be neglected. For the accuracy of this method, the temperature dependent material properties (heat conduction, heat capacity, and density) have to be well known in the temperature range of $300 < T < 600$ K.

In Fig. 5, analytical temperature distributions over time have been used to verify the data reduction tool. The calculated heat flux values match the analytical results very well. The use of a C^{++} based program reduced the interpretation time for one test run from hours to minutes.

Once the convective heat flux is known, the dimensionless Stanton number, defined as

$$St = \frac{\dot{q}_{\text{conv}}}{\rho_\infty v_\infty c_{P,\text{air}}(T_{\text{rec}} - T_w)} \tag{8}$$

can be calculated. The recovery factor to calculate the recovery temperature is $r = 0.9$ and the recovery temperature is defined as

$$T_{\text{rec}} = \left(1 + r\frac{\kappa - 1}{2}M_\infty^2\right)T_\infty \tag{9}$$

IV. Experimental Results

The goals of the recent experimental program were twofold:

1) To measure the effects of the integrated passive boundary-layer bleed at the location of the lip shock impingement on pressure distribution, Mach number distribution, and combustion chamber mass flow.

2) To study the application of the infrared thermography and calculate the Stanton number on the isolator sidewalls.

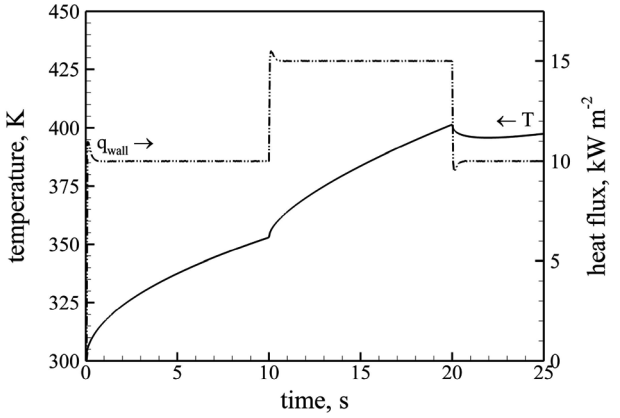

a) Boundary condition of the second kind 10-15-10 kW/m^2

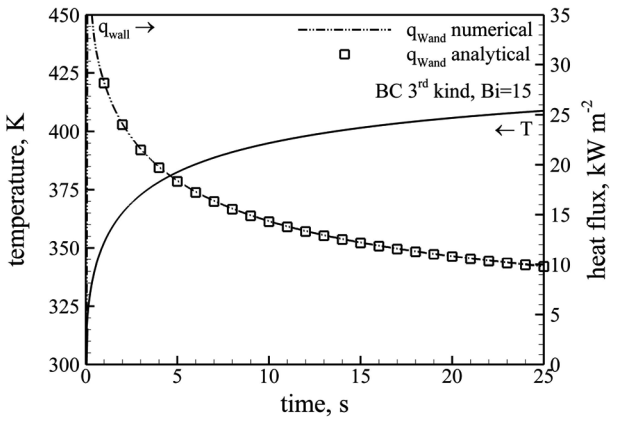

b) Boundary condition of the third kind

Fig. 5 Validation of the used data reduction procedure to evaluate the Stanton number.

The following section is divided into two main subsections. First, the results without imposed backpressure by the mass flow meter are discussed. Thereafter, the effects of increasing the simulated combustion chamber backpressure on the internal flowfield structure are analyzed.

A. No Backpressure

1. *Pressure and Schlieren Pictures*

The first results to be discussed are the wall pressure distribution along the upper and lower isolator walls as shown in Fig. 6. The first diagram, Fig. 6a, shows the normalized pressure distribution for the configuration without boundary-layer bleed. The pressure level of the first static pressure port on the upper wall of the isolator is significantly higher than the calculated value by means of a characteristic approach (MOC) [24]. This indicates that the effective cross section of the throat is considerably smaller than the geometrical cross section, a consequence of the existing separation bubble in this area.

In contrast to the first diagram, Fig. 6b shows the effect of introducing a passive boundary-layer bleed on the viscous flow structure. The normalized pressure level of the first pressure port equals the predicted value of the characteristic method. This implies that the shape of the lip shock is as calculated by the MOC and that no boundary-layer separation on the ramp occurs. The comparison of these two diagrams shows the effectiveness of controlling the boundary-layer and the shock–boundary-layer interaction with the chosen design.

The change of the shock structure in the throat, i.e., complex shock–boundary-layer interaction with λ-shock, shock–shock interaction, etc., [25] compared with a single lip shock, and the reduced mass flow in the isolator due to the removed mass flow by the passive bleed, lead to a different reflected shock structure in the

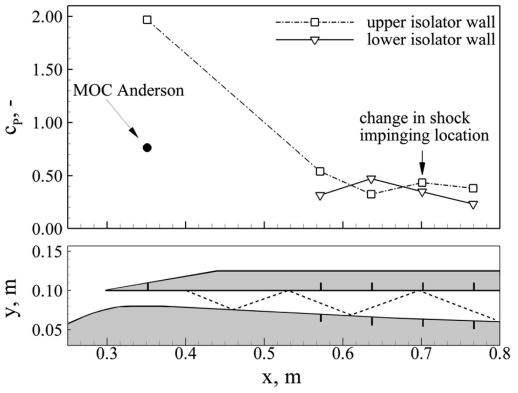

a) Static wall pressure coefficient without bleed

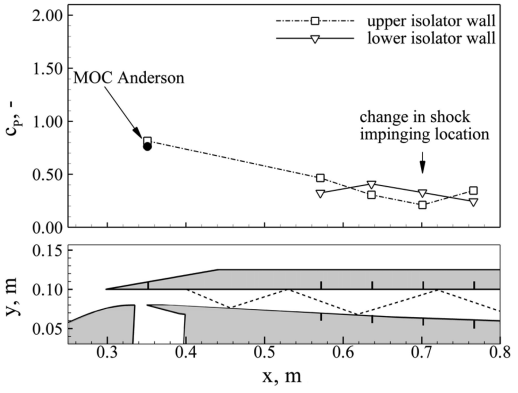

b) Static wall pressure coefficient with bleed

Fig. 6 Comparison of static wall pressure coefficient in the isolator with and without bleed including theoretical pressure value computed by MOC [24], reflected shock structure (schematically).

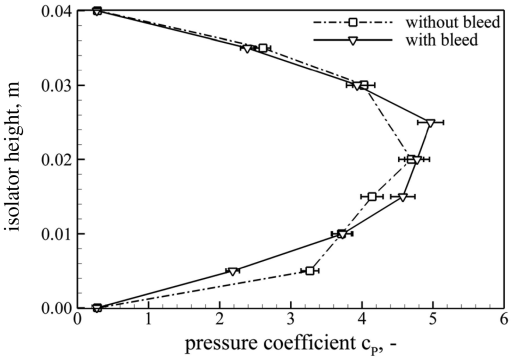

a) c_P pitot rake

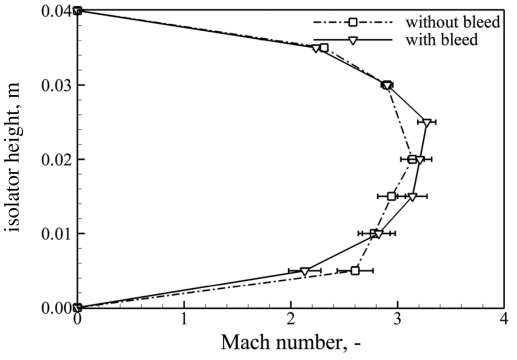

b) Calculated Mach number pitot rake

Fig. 7 Comparison of pitot pressure and calculated Mach number profiles over height of the isolator exit for the configuration without and with bleed.

isolator. This can be seen by comparing the downstream pressure ports in Figs. 6a and 6b. Even though the geometrical resolution is limited, a change in axial pressure distribution is visible. The static pressure values at the location $x = 0.700$ m have changed. In Fig. 6a, the upper wall pressure value is higher than the lower wall value, indicating that the reflected shock impinges on the upper wall before the pressure port at location $x = 0.700$ m. In contrast to that, in Fig. 6b, the upper wall pressure value is still decreasing, indicating that the reflected shock is impinging on the upper wall after the pressure port location $x = 0.700$ m.

Despite the existence of the boundary-layer separation in the inlet throat area, which increases the effective internal compression and causes the concern that the inlet is likely to unstart, both configurations did self-start. This can be seen by comparing the pitot pressure measurements and Mach number profiles at the isolator exit (Fig. 7), and the captured mass flows shown in Table 2.

The pitot results show comparable dimensionless pitot pressure and Mach number distributions over the height of the isolator exit at $x = 0.800$ m. As mentioned earlier, the isolator has a diverging angle of -3 deg due to the previous design. This fact, along with the relatively high throat Mach number, leads to a maximum Mach number of about $M = 3$ at the isolator exit plane.

In Table 2, the breakdown of the different mass flows is shown. The captured mass flow for the started inlet at design Mach number $M = 6$ and no boundary-layer bleed is $\dot{m}_3/\dot{m}_0 = 0.915$; the spill is consequently $\dot{m}_{\text{spill}}/\dot{m}_0 = 0.085$. The existing spillage occurring even for the shock on lip Mach number is due to the displacement effects of the developing boundary layers on the ramps and the side walls. With the aid of CFD calculations, the influence of the viscous flow on the spillage compared with MOC design could be demonstrated. Table 2 shows the calculated spill for a two-dimensional k–ω–SST calculation accomplished with the commercial CFD tool FLUENT and for a three-dimensional Speziale, Sarkar, and Gatski (SSG) turbulence model calculation [18] accomplished with the FLOWer code. The viscous effect of the ramps only (two-dimensional calculation) results in a spill of $\dot{m}_{\text{spill}}/\dot{m}_0 = 0.05$. This is based on the displacement thickness of the boundary layer, resulting in a steeper effective ramp angle and, in succession, steeper shock angles passing the lip further upstream. In addition, each sidewall introduces a weak shock due to the developing boundary layer and complex corner flows emerge from the ramp and the sidewall boundary layer [26]. All this leads to an increased spill of $\dot{m}_{\text{spill}}/\dot{m}_0 = 0.092$ in total, which is in good agreement to the measured value.

Because the inlet did not block for either configuration, the spill is assumed to be identical for both configurations. This leads to the result that the removed mass flow by the passive bleed is on the order of $\dot{m}_{\text{bleed}}/\dot{m}_0 = 0.055$, as shown in Table 2.

2. *Infrared Measurements*

One major goal of this measurement campaign was the application of the infrared thermography to the isolator side walls. This is accomplished by inserting a material with weak heat conductivity, i.e., PEEK, into the window location of one of the inlet side walls and an infrared (IR) permeable window (ZnS) on the other side wall. Because the IR camera is located inside the wind-tunnel chamber,

Table 2 Breakdown of the different inlet mass flows and total pressure recovery

Mass flow rate, $\dot{m}_3/\dot{m}_0$				Total pressure recovery
Combustion chamber	Bleed	Spill		p_{t3}/p_{t0}
$0.915 \pm 2.8\%$	0	≈ 0.085	0.05 CFD two-dimensional 0.092 CFD three-dimensional [18]	0.1597
$0.860 \pm 2.9\%$	≈ 0.055	≈ 0.085	——	0.167

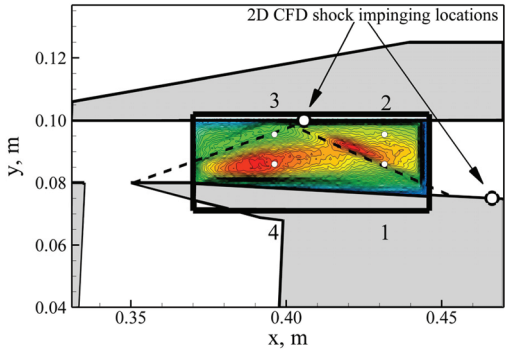

a) First window

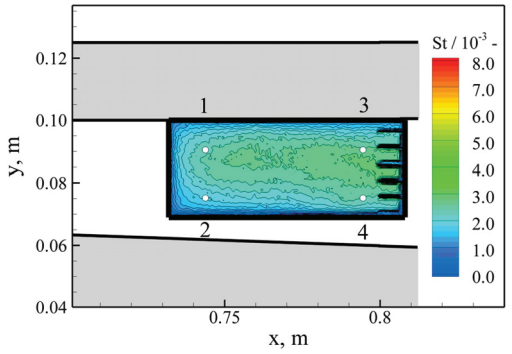

b) Second window

Fig. 8 Stanton number distribution on inner side wall of isolator.

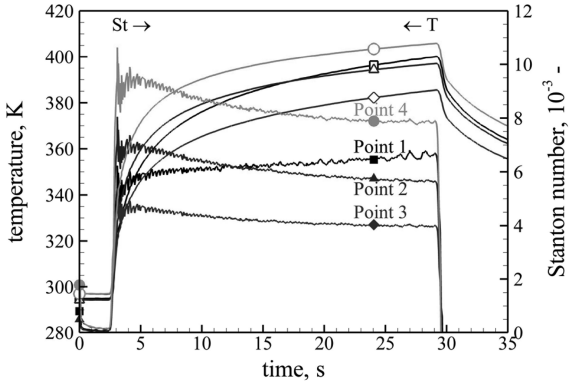

a) First window

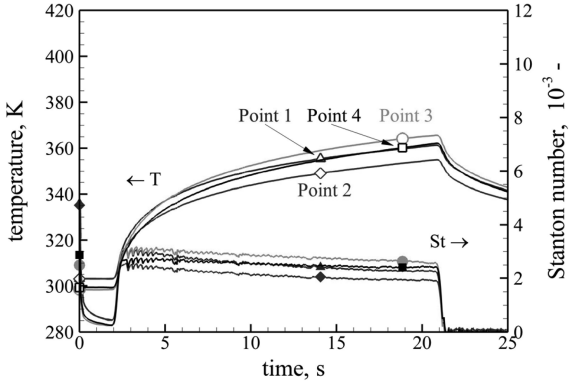

b) Second window

Fig. 9 Time history of surface temperature and Stanton number for discrete points on inner side wall of isolator.

two IR windows are placed in front of the camera, requiring a calibration of the complete optical path in front of a blackbody radiator to evaluate the accurate transmittance and correct existing disturbances, i.e., reflections.

The Stanton number distribution on the side wall is shown in Fig. 8. In Fig. 8a, the Stanton number subsequent to the throat area is shown. The absolute values of the Stanton number are considerably higher than the values at the exit of the isolator in Fig. 8b. This is based on the fact that the pressure is higher and the boundary-layer thickness is smaller, hence the thermal boundary-layer thickness is smaller and the temperature gradient is higher than in the downstream region. Both facts lead to a higher heat transfer coefficient.

Furthermore, the change in heat transfer coefficient based on the shock structure leading to different wall pressure distribution and boundary-layer thickness can be seen in Fig. 8a. The theoretical shock structure is indicated by the two dashed lines. The first internal shock forms at the corner of the boundary-layer bleed gap. This is due to the fact that the lip shock turns the flow far in excess of the horizontal direction, leading to a negative velocity component in the y direction.

The second shock is the reflection of the first shock at the upper wall of the isolator. In addition, the impinging locations of the shock as predicted by the two-dimensional CFD analysis are shown. The shocks are steeper due to the three-dimensional effects, i.e., side wall boundary layer, corner flows, etc., unaccounted for in the two-dimensional calculation.

The temperature development and the corresponding Stanton number history for four specific pixels are shown in Fig. 9. The positions are marked and labeled in Fig. 8. The lower diagram (Fig. 9b) especially shows a nearly constant Stanton number over time as expected for constant heat transfer coefficients. However, the Stanton numbers in the upper diagram (Fig. 9a) approach an almost constant value at the end of the test run, too. The gradually decreasing Stanton number history during each test run indicates that the heat transfer coefficient to the side wall, especially at the beginning of each test run, is not constant. The reason for this effect has to be investigated in more detail; one reason is the great change of the ratio between wall temperature and recovery temperature.

In theory, for a constant heat transfer coefficient, the wall heat flux decrease due to the rising wall temperature and this is considered by the decrease of temperature (enthalpy) difference in the calculation of the Stanton number [Eq. (8)]. At the beginning of a test run this is not true, especially since the wall temperature change is very strong, which results in a thickening of the thermal boundary layer, leading to a strong change in temperature distribution within the boundary layer, i.e., location and value of the maximum temperature, wall temperature [27], and thus a change in the heat transfer coefficient.

To check the feasibility of the measured surface temperatures and the calculated Stanton numbers, the analytical surface temperature development of a plate (transient Fourier equation) and boundary condition of the third kind [28], i.e., constant heat transfer coefficient over time, are compared with the measured values. The Biot number, describing the heat transfer, is varied until the sum of the mean square root is minimized. The results of this approach are shown in Fig. 10 for the same pixel locations as before. The computed temperature curves match the measured ones quite well, for the first window as well as for the second window.

The differences in wall temperature distribution over time are small, as can be seen in Fig. 10. But Fig. 10a, especially the line corresponding to point 4 (circle), shows that for the analytical solution with a constant heat transfer coefficient, the temperature is below the measured values in the first 10 s. In contrast, the measured temperature rises faster and to a higher value in this time interval. This is due to the previously mentioned higher heat transfer coefficient at the beginning.

From the Biot number, the heat transfer coefficient and thus the Stanton number can be calculated. Both are listed in Table 3. The calculated Stanton numbers are in good agreement to the values at the end of each test run as shown in Fig. 9.

At room temperature, $\tau_{\text{total}} = 0.48$ has been calibrated in front of a blackbody radiator. Because it is possible to match the measured temperature development over time with analytical methods, the transmittance coefficient cannot vary in a great range. The assumption of a constant transmittance coefficient is consolidated by

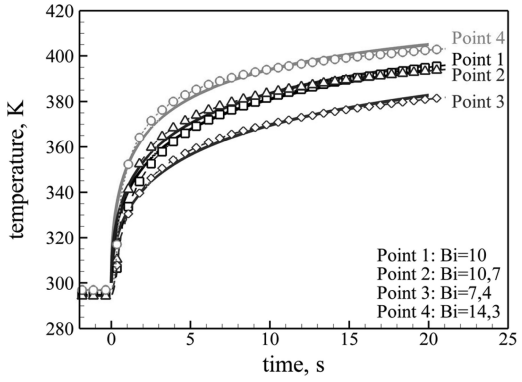

a) First window

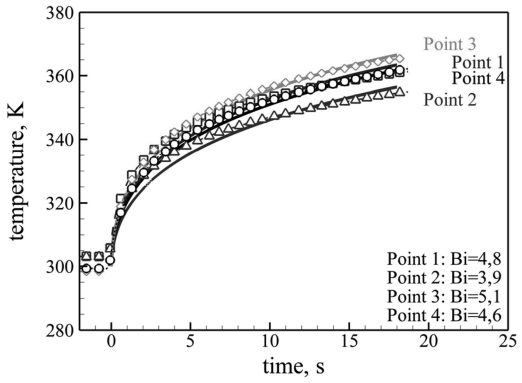

b) Second window

Fig. 10 Comparison of measured and analytically calculated time histories of surface temperature.

looking at the results from Hawkins and Hunneman [29]; also the investigated wavelength is in the range of 10–20 μm and in a temperature range of 50–300 K. Using conservative assumptions for the emissivity of PEEK $\varepsilon = 0.95 \pm 2.5\%$ and $\tau_{\text{total}} = 0.48 \pm 2\%$, the measured surface temperature accuracy is on the order of $\pm 1\%$ based on the wall temperature in Kelvin.

For the convective heat flux calculation, the absolute temperature is noncritical, the temperature gradient over time is the driving parameter, and this value is measured with a higher accuracy. A sensitivity analysis has been performed for the Stanton number accuracy using material data and wind-tunnel conditions. The result shows that for the worst case of maximum error in all parameters, the overall accuracy of the calculated Stanton number is close to $\pm 25\%$ ($\pm 5\%$ for convective heat flux itself) and is especially sensitive to the temperature difference ($T_{\text{rec}} - T_{\text{wall}}$) but with different algebraic signs for the error of each of the two temperatures. Because in reality single errors never occur simultaneously and, in addition, have different algebraic signs, the presented measurement results are much more accurate.

Table 3 Stanton numbers calculated from the analytically achieved Biot numbers

$T_m = 369.5$, K	$\lambda_m = 0.264$, $\text{Wm}^{-1}\text{K}^{-1}$	$d = 0.012$, m	
Point	Biot number	α, $\text{Wm}^{-2}\text{K}^{-1}$	St number
	First window		
1	10.0	220.0	$5.36 \cdot 10^{-3}$
2	10.7	235.7	$5.74 \cdot 10^{-3}$
3	7.4	162.8	$3.97 \cdot 10^{-3}$
4	14.3	314.6	$7.66 \cdot 10^{-3}$
	Second window		
1	4.8	105.6	$2.57 \cdot 10^{-3}$
2	3.9	85.8	$2.09 \cdot 10^{-3}$
3	5.1	112.2	$2.73 \cdot 10^{-3}$
4	4.6	101.2	$2.46 \cdot 10^{-3}$

For the maximum and minimum Stanton numbers of about $St_{\max} = 0.008$ and $St_{\min} = 0.004$ at the inlet throat location, the expected free-flight wall heat flux, assuming a regenerative cooled wall ($T_{\text{wall}} = 300$ K), is calculated for two different Mach numbers and compared with the measured results of Kanda et al. [17] (see Table 4). The assumed altitude is 25,000 m, corresponding to the mentioned flight condition of Mach 6 and dynamic pressure of 64 kPa; at this altitude, the needed freestream conditions are calculated. This free-flight condition is matched according to [17] by the selected wind-tunnel conditions reported in Kanda et al. and are also listed in Table 4.

Of course, the configurations differ because Kanda et al. [17] investigated a side wall compression inlet and the present configuration is a classical two-dimensional inlet, making the comparison difficult. However, from a geometrical point of view, the ratio of capture to throat area is similar and the heat loads in the region of the throat are in the same order [16,17].

B. With Backpressure

1. Pressure and Schlieren Pictures

The following section focuses on the variation of the flow structure in the rear part of the isolator. To discuss the effects of increasing backpressure, schlieren pictures and pitot pressure profiles are shown. In a supersonic flow, due to the hyperbolic character of the differential equation, pressure changes cannot propagate upstream. Because the flow in the boundary layer eventually decelerates to subsonic velocity, thereby changing the character of the governing equations, the pressure rise propagates upstream in the subsonic region of the boundary layer.

A positive pressure gradient forces the boundary layer to thicken and ultimately to separate. In both cases, a boundary-layer-induced shock develops. Because of the geometrical shape of the isolator, the pressure on the lower side of the isolator is slightly smaller than on the upper side. This leads to the effect that the backpressure propagates further upstream on the lower side of the isolator.

In Fig. 11, a sequence of schlieren pictures and the corresponding pitot profiles are shown for different backpressures, increasing from top to bottom for the configuration with bleed in the inlet throat. Figure 11a shows the situation with no additionally imposed backpressure, i.e., $p/p_\infty = 10(\Delta = 40\%)$. The reflected lip shock is visible in the schlieren picture as well as the detached shocks in front of the visible pitot tubes P1–P5 (P6 and P7 are not visible in the window), indicating supersonic flow. The pitot pressure and the calculated Mach number profile are also shown. The both profiles are almost symmetrical to the centerline.

The next set, Fig. 11b, shows the situation at a pressure ratio of $p/p_\infty = 16(\Delta = 44\%)$. The shock induced by the thickening of the lower boundary layer is visible in the lower right part of the schlieren picture. A second boundary-layer-induced shock can be seen in the upper right part of the schlieren picture but further downstream than the lower one. This is an effect of the different wall pressure distribution due to the reflected shock system and geometry constraints. The pitot pressure profile also shows that the

Table 4 Calculated wall heat fluxes for two free flight conditions based on measured Stanton numbers and comparison to measured wind-tunnel heat flux values [17]

	M_∞	T_{t0}, K	p_{t0}, kPa	q_∞, kPa	T, K	ρ_∞, kgm^{-3}	u_∞, ms^{-1}	Wall heat flux, MWm^{-2}	
Free-flight condition	6	1820	3965	64	1660	0.0395	1790	0.385–0.77	present study
Free-flight condition	7	2293	10,396	86	2180	0.0395	2089	0.625–1.25	present study
Wind tunnel	5.3	1550	4780	126	1420	0.09535	1626	0.30–0.50	[17]

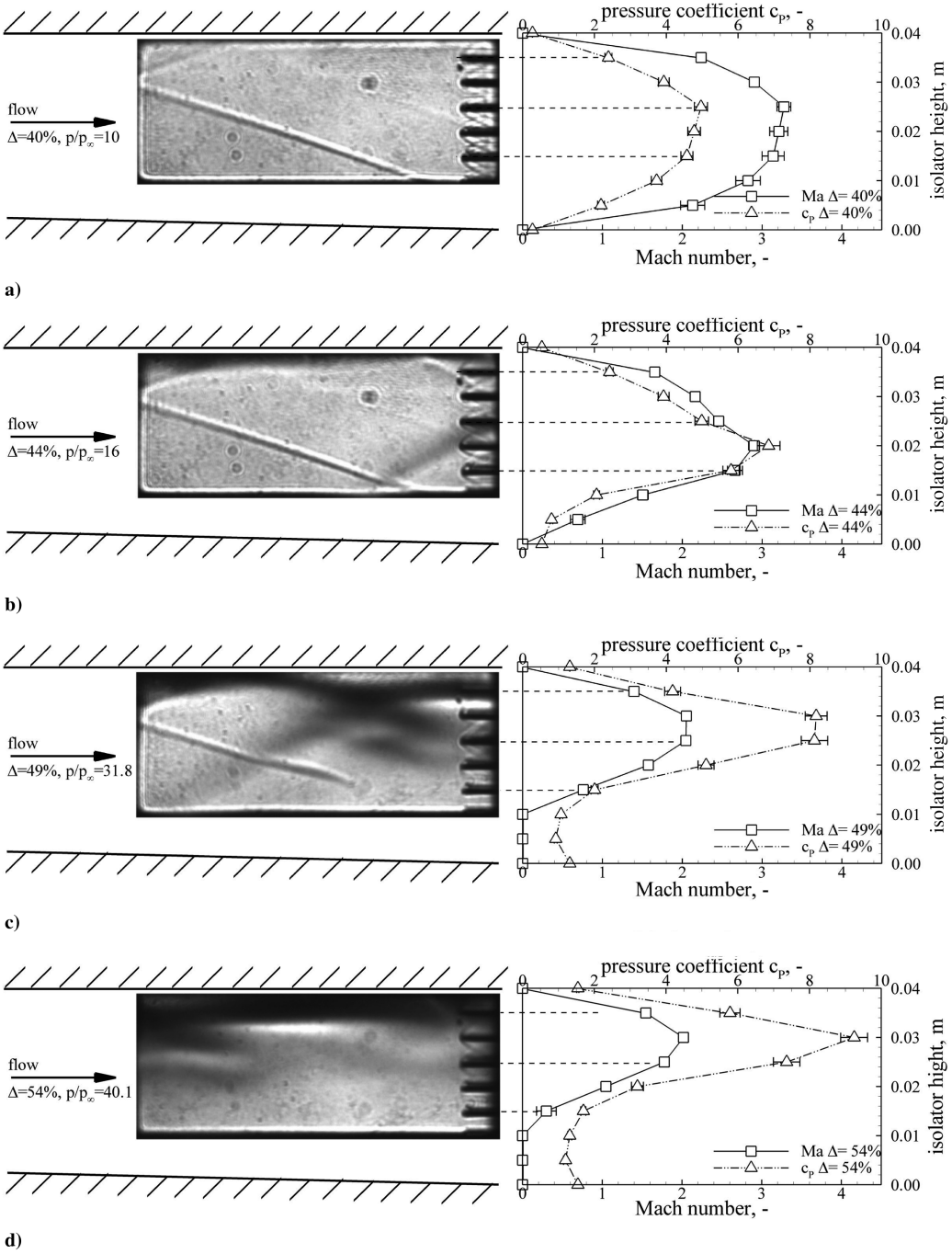

Fig. 11 Schlieren pictures of second window on the left compared with pitot pressure and Mach number profiles on the right for different throttling degrees.

boundary-layer thickness increases more on the lower side of the isolator. The pitot pressures of the two lower ports decrease compared with the preceding situation.

Increasing the backpressure ratio to $p/p_\infty = 31.8(\Delta = 49\%)$ leads to a further upstream propagation of the pressure rise, as shown in Fig. 11c. The shock located in the right lower part of the preceding picture has moved upstream to the left corner of the window. This shock now clearly interacts with the reflected lip shock and both shocks are bent toward the centerline. The boundary-layer-induced shock also interacts with the upper wall boundary layer. This impinging shock leads to a boundary-layer separation due to the resulting strong positive pressure gradient [25,30]. The reflected lip shock interacts with the lower boundary-layer/separation region. In this case, however, the shock vanishes, which proves the existence of a thick subsonic boundary layer at this point. The reflected expansion waves are not visible in the schlieren picture. The pitot profiles also show that a large region of the isolator height is already subsonic.

Further increasing the backpressure ratio to $p/p_\infty = 40.1(\Delta = 54\%)$ causes the previously described shock structure to move further upstream out of the visible area of the windows. The subsonic region covers the bottom half of the isolator. The shock structure within the supersonic jet in the upper half cannot be visualized in the current schlieren pictures, except two bow shocks in front of pitot pressure port P2 and P3.

2. *Infrared Measurement*

The infrared thermography has also been used to investigate the flow structure at different imposed backpressures, because the heat transfer coefficient should change with changing flow structure. Fig. 12 shows the measured temperature and calculated Stanton number development over time for four distinct points. During this wind-tunnel run, three backpressure ratios, i.e., $p/p_\infty = 10(\Delta = 40\%)$, $p/p_\infty = 17(\Delta = 45\%)$, and $p/p_\infty =$

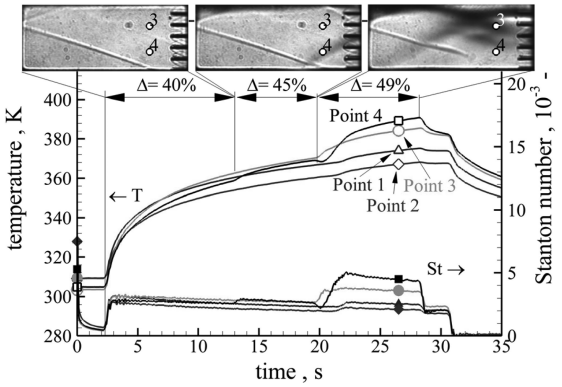

Fig. 12 Measured wall temperature and calculated Stanton number development over time for three different throttle degrees, corresponding schlieren pictures.

$31.8(\Delta = 49\%)$, were simulated. The schlieren pictures of the corresponding conditions with the location of the interesting points (points 3 and 4) are placed above the temperature and Stanton number plot.

For the backpressure ratio $p/p_\infty = 10(\Delta = 40\%)$, the calculated Stanton numbers for all four locations and especially for the two discussed locations (points 3 and 4) have approximately the same value. Increasing the backpressure ratio to $p/p_\infty = 17(\Delta = 45\%)$ leaves the line corresponding to point 3 unaffected. The temperature development does not show any discontinuity and thus the Stanton number is also unchanged. In contrast to this, the temperature development over time at the location corresponding to point 4 increases slightly, resulting in an increase in Stanton number value ($13 < \text{time} < 19$ s). Looking at the schlieren picture for this backpressure ratio shows that the lower location (point 4) is already in an area affected by the increased backpressure. In evidence is the boundary-layer-induced shock in the lower right corner of the window. For the next backpressure ratio, $p/p_\infty = 31.8(\Delta = 49\%)$, the change in temperature and Stanton number development over time is clearly visible, for both locations. The lower location (point 4) is already in the subsonic flow regime (schlieren picture) which results in a considerable increase in temperature and thus in an increased Stanton number. In addition, for this flow situation, the upper location (point 3) is also affected by the backpressure rise, resulting in a moderate Stanton number increase at this location.

For two backpressure ratios, the schlieren pictures are compared with the wall Stanton number distribution (see Fig. 13). Although the schlieren method is a line-of-sight measurement technique [20] and the Stanton number calculation is based on the measured wall temperature, the principal change in flow structure is visible. Figure 13a shows the flow structure for a backpressure ratio of $p/p_\infty = 31.8(\Delta = 49\%)$; especially the region with subsonic flow regime in the lower right part of the window and the shock-induced boundary-layer separation on the upper wall of the internal flowpath is visible in the schlieren picture and also visible in the Stanton number distribution. Increasing the backpressure ratio to $p/p_\infty = 40.1(\Delta = 54\%)$ leads to an upstream propagation of the shock-induced boundary-layer separation and to an increased area of subsonic flow in the lower part of the window (see Fig. 13b). The change in flow structure is also visible in the Stanton number distribution, because the high-heat load area of the separation bubble has disappeared and the high-heat load area based on the subsonic flow regime has increased.

Finally, the effects of very high backpressure ratios to the flowfield in the area of the inlet throat (first window) are discussed. For throttle degrees exceeding $\Delta = 67\%$, the flow at the exit of the internal flowpath is already completely subsonic. For a backpressure ratio up to $p/p_\infty = 92(\Delta = 75\%)$, the flow structure at the first window location right behind the inlet throat is unchanged, as can be seen in Fig. 14a. Increasing the backpressure ratio to $p/p_\infty = 128(\Delta = 81\%)$ causes the flow structure to completely change. The pattern of the Stanton number distribution, which could be matched to the

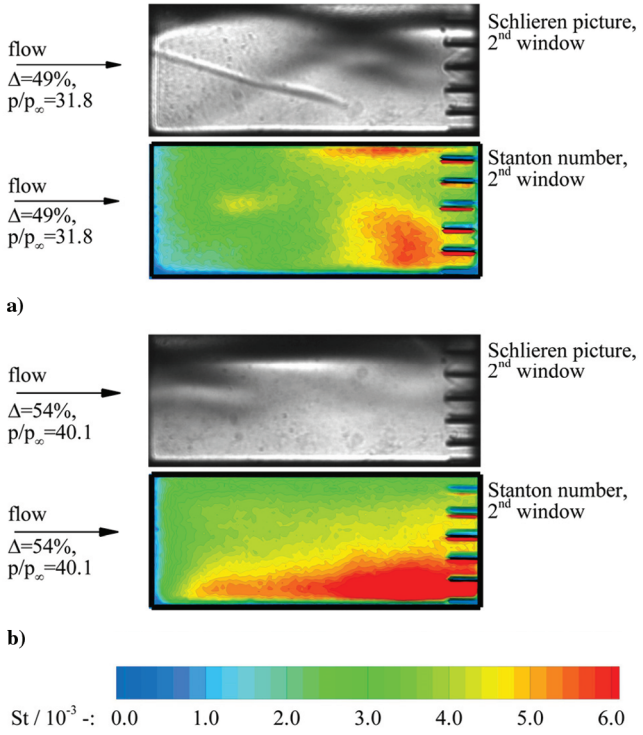

Fig. 13 Comparison of schlieren pictures and calculated Stanton number distribution for two different throttle degrees.

reflected shock system for the previous situation, changes completely. The overall value of the Stanton number increases and there is a region of considerably high Stanton numbers developing at the lower left corner of the window and horizontally propagating downstream (see Fig. 14b). This could be a vortex system near the wall starting at the location of the now present normal shock. The normal shock must be located in the region between the passive bleed

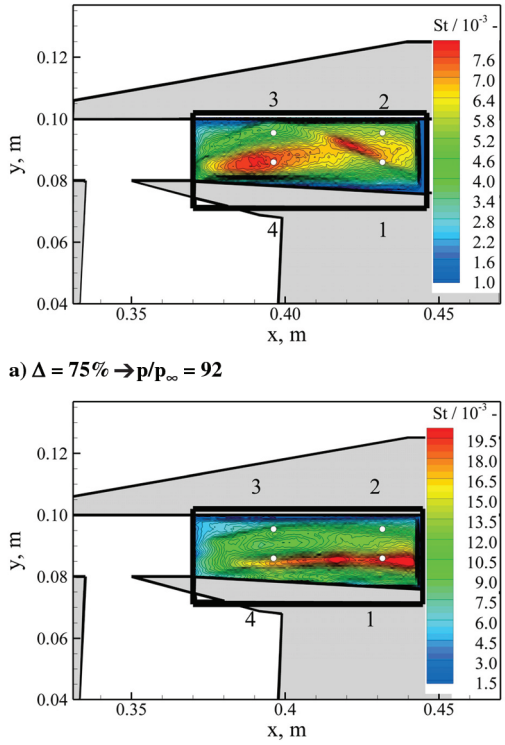

Fig. 14 Calculated Stanton number distribution at the location of the 1st window, configuration with bleed, two different throttle degrees.

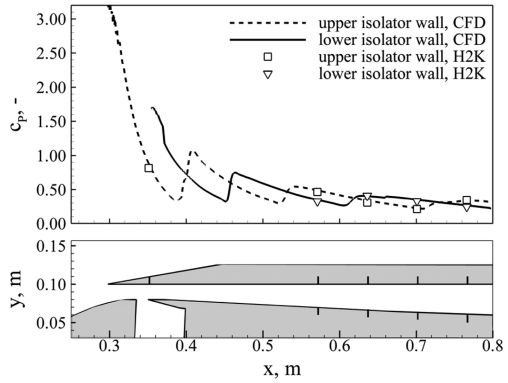

Fig. 15 Comparison between numerical wall pressure distribution and measured values for the configuration with bleed.

and the left window edge, because the value of the first pressure port is unchanged for the investigated backpressure ratios and is always in good agreement to the predicted value by the method of characteristics, as seen in Fig. 6b. This phenomenon will be investigated in more detail during a future measurement campaign.

C. Comparison of Experimental and Numerical Results

The experimental data are compared with CFD calculations performed with the commercial tool FLUENT. The unstructured grid is two-dimensional with a structured subgrid near the walls. The fluid is air with the assumption of a caloric-perfect gas with $\gamma = 1.4$. The integrated two-equation turbulence plasma model k–ω–SST was used. The structured subgrid satisfies the criteria of a y^+ value on the order of one near the wall, resolving the laminar sublayer.

Figure 15 shows good agreement between the calculated wall pressure coefficient distribution and the measured values for the configuration with bleed. The alternating change in pressure level between the upper and lower surface of the isolator is reproduced. But based on the few pressure ports available, it is not possible to check if the shock impinging locations are calculated adequately. Because it is a two-dimensional calculation and three-dimensional effects are not considered, the shock structure will differ.

Detailed two- and three-dimensional numerical calculations of the inlet model are performed by Krause et al. [18]. Calculations for the configuration without and with passive bleed based on an advanced turbulent model (SSG-model) with seven equations did result in fully converged solutions for both configurations. The wall pressure coefficients of the three-dimensional computations agree well with the measured values shown in Figs. 6a and 6b. The first static pressure port indicating the separation bubble for the configuration without bleed is especially met very well [18].

V. Conclusions

An experimental study has been performed to achieve a better understanding of the viscous flow effects including the aerothermodynamic heating in the internal flowpath of a scramjet compression system. This has been performed with respect to the performance of the inlet and isolator of a scramjet propulsion unit depending on its operation mode, i.e., different simulated backpressures. The positive influence of the integration of a passive bleed has been verified and the concept could be proven. Further, the infrared surface temperature measurement technique was successfully applied to calculate the heat transfer coefficient to the isolator side walls.

It could be demonstrated that the passive bleed reduces the separation bubble significantly, with limited mass flow rate penalty. In contrast to previous assumptions, the inlet starts for both configurations with and without boundary-layer bleed. The bleed presence does not remarkably influence the pitot pressure profile and the Mach profile at the end of the isolator. But the flow structures in the inlet throat area are completely different. The resulting downstream effects in the isolator have to be further investigated. The application of the infrared thermography on the isolator side walls allowed the calculation of the heat transfer coefficient. Especially, the two-dimensional distribution of the heat loads due to the flow structure (i.e., shocks, varying backpressure ratios) could be resolved.

Acknowledgments

The financial support by the German National Research Council (DFG) within the Graduate College "Aerothermodynamic Design of a SCRAM-Jet Propulsion System for Future Space Transportation" and the German Aerospace Center Cologne is gratefully acknowledged. We would further like to thank P. Herzog and M. Janke for their assistance during the experiments and A. Henckels and P. Gruhn for the technical discussions on the test results. Furthermore, we thank D. Gohlke for implementing the new C^{++} heat flux calculation tool.

References

[1] Voland, R. T., Rock, K. E., Huebner, L. D., Witte, D. W., Fischer, K. E., McClinton, C. R., "Hyper-X Engine Design and Ground Test Program," *AIAA 8th International Space Planes and Hypersonic Systems and Technologies Conference*, AIAA Paper 98-1532, 1998.

[2] Weigand, B., Gaisbauer, U., Reinatz, B., Kau, H.-P., and Schröder, W., "Das Graduiertenkolleg 1095/1: Aerothermodynamische Auslegung eines SCRAM-Jet-Antriebssystems für zukünftige Raumtransportsysteme," Deutscher Luft- und Raumfahrtkongress, Braunschweig, 2006.

[3] Fry, R. S., "A Century of Ramjet Propulsion Technology Evolution," *Journal of Propulsion and Power*, Vol. 20, No. 1, 2004, pp. 27–58.

[4] Billig, F. S., and Kothari, A. P., "Streamline Tracing: Technique for Designing Hypersonic Vehicles," *Journal of Propulsion and Power*, Vol. 16, No. 3, 2000, pp. 465–471.

[5] Billig, F. S., "Research on Supersonic Combustion," *Journal of Propulsion and Power*, Vol. 9, No. 4, 1993, p. 499.

[6] Heiser, W. H., Pratt, D. T., *Hypersonic Airbreathing Propulsion*, AIAA Education Series, AIAA, Washington, D.C., 1993.

[7] Emami, S., Trexler, C. A., Auslender, A. H., and Weidner, J. P., "Experimental Investigation of Inlet-Combustor Isolators for a Dual Mode Scramjet at a Mach Number of 4," NASA TP 3502, May 1995.

[8] Herrmann, C. D., and Koschel, W. W., "Experimental Investigation of the Internal Compression of a Hypersonic Intake," AIAA Paper 2002-4130, 2002.

[9] Reinartz, B. U., Herrmann, C. D., Ballmann, J., and Koschel, W. W., "Aerodynamic Performance Analysis of a Hypersonic Inlet Isolator Using Computation and Experiment," *Journal of Propulsion and Power*, Vol. 19, No. 5, 2003, pp. 868–875.

[10] Sugiyama, H., and Minato, R., "Study on Shock Wave and Turbulent Boundary Layer Interactions in a Square Duct at Mach 2 and 4," *Journal of Thermal Science*, Vol. 15, No. 1, 2006, pp. 37–42.

[11] Van Driest, E. R., "Investigation of Laminar Boundary Layer in Compressible Fluids Using the Crocco Method," NACA TN 2597, 1952.

[12] Mitani, T., Sakuranaka, N., Tomioka, S., and Kobayashi, K., "Boundary-Layer Control in Mach 4 and Mach 6 Scramjet Engines," *Journal of Propulsion and Power*, Vol. 21, No. 4, 2005, pp. 636–641.

[13] Shih, T. I.-P., Rimlinger, M. J., and Chyu, W. J., "Three Dimensional Shock-Wave/Boundary-Layer Interactions with Bleed," *AIAA Journal*, Vol. 31, No. 10, 1993, pp. 1819–1826.

[14] Harloff, G. J., and Smith, G. E., "Supersonic-Inlet Boundary-Layer Bleed Flow," *AIAA Journal*, Vol. 34, No. 4, April 1996, pp. 778–785.

[15] Enomoto, Y., Kimura, H., Fujiwara, K. K, Fujimoto, A., Mitani, T., and Yanagi, R., "Experimental Study of Mach 5 Fixed Geometry Inlet for Subscale Ramjet Engine Test," International Symposium on Air Breathing Engines Paper 97-7032, 1997.

[16] Kouchi, T., Mitani, T., and Masuya, G., "Numerical Simulations in Scramjet Combustion with Boundary-Layer Bleeding," *Journal of Propulsion and Power*, Vol. 21, No. 4, 2005, pp. 642–649.

[17] Kanda, T., Hiraiwa, T., Mitani, T., Tomioka, S., and Chinzei, N., "Mach 6 Testing of a Scramjet Engine Model," *Journal of Propulsion and Power*, Vol. 13, No. 4, 1997, pp. 543–551.

[18] Krause, M., Reinartz, B., and Ballmann, J., "Numerical Computations for Designing a Scramjet Engine," International Council of the Aeronautical Sciences (ICAS) Paper No. 194, 2006.

[19] Kantrowitz, A., and Donaldson, C. duP., "Preliminary Investigation of Supersonic Diffusers," NACA ACR No. L5D20, 1945.

[20] Merzkirch, W., *Flow Visualisation*, ISBN 0-12-491350-4, Academic Press, New York, 1974.
[21] Triesch, K., "Verwendung von Kegeldüsen zur Drosselung und Durchsatzmessung bei Überschalleinläufen," German Aerospace Center (DLR), IB-39113-83-A-04, 1983.
[22] Henckels, A., and Gruhn, P., "Study on Aerothermal Effects of Viscous Shock Interaction in Hypersonic Inlets," *Proceedings of the Fifth European Symposium on Aerothermodynamics for Space Vehicles*, German Aerospace Center, Wind Tunnel Dept., Cologne, Germany, 2005, pp. 553–558.
[23] ThermaCAM SC-3000 Manual, FLIR Systems, Portland, OR, June 1999.
[24] Anderson, B. H., "Design of Supersonic Inlets by a Computer Program Incorporating the Method of Characteristics," NASA TN-D-4960, 1968.
[25] Delery, J., "Shock/Shock and Shock-Wave/Boundary-Layer Interactions in Hypersonic Flows," AGARD, FDP-VKI, May–June 1988.
[26] Schepers, H. J., "Flow and Heat Transfer Measurements in Corner Regions at Hypersonic Speeds," German Aerospace Center (DLR), FB 76-02, 1976.
[27] Van Driest, E. R., "Turbulent Boundary Layer in Compressible Fluids," *Journal of the Aeronautical Sciences*, Vol. 18, No. 3, March 1951, pp. 145–160.
[28] Wärmeatlas, *Berechnungsblätter für den Wärmeübergang*, 5th ed., VDI-Verlag, GmBH, Düsseldorf, Germany, ISBN 3-18-400760-X, 1988.
[29] Hawkins, G., and Hunneman, R., "The Temperature-Dependent Spectral Properties of Filter Substrate Materials in the Far-Infrared (6–40 μm)", *Infrared Physics and Technology*, Vol. 45, No. 1, 2004, pp. 69–79.
[30] Edney, B. E., "Effects of Shock Impingement on the Heat Transfer Around Blunt Bodies," *AIAA Journal*, Vol. 6, No. 1, 1986, pp. 15–21.

R. Bowersox
Associate Editor